

Dispersive wave propagation in disordered flexible fibers enhances stress attenuation

Peng Wang,¹ Thomas Pähzt,² Kun Luo,³ and Yu Guo^{1,3,4,*}

¹*Department of Engineering Mechanics, Zhejiang University, Hangzhou 310027, China*

²*Institute of Port, Coastal and Offshore Engineering, Ocean College, Zhejiang University, Zhoushan 316021, China*

³*State Key Laboratory of Clean Energy Utilization, Zhejiang University, Hangzhou 310027, China*

⁴*Huanjiang Laboratory, Zhuji, Zhejiang Province 311800, China*



(Received 17 September 2024; accepted 16 December 2024; published 9 January 2025)

We experimentally and computationally analyze impact-shock-induced stress wave propagation in packings of disordered flexible fibers. We find that dispersive wave propagation, associated with large stress attenuation, occurs much more prevalently in systems with larger fiber aspect ratios and moderate fiber flexibility. We trace these features to the microstructural properties of fiber contact chains and the energy-trapping abilities of deformable fibers. These findings provide insights into physics of the shock-impacted flexible fiber packings and open the way toward an improved granular-material-based damping technology.

DOI: [10.1103/PhysRevE.111.015412](https://doi.org/10.1103/PhysRevE.111.015412)

I. INTRODUCTION

When a granular medium is hit by a shock, stress waves are generated and propagate within it through the network of interparticle contacts. Due to significant energy dissipation via the inelastic and sliding frictional contacts in this dynamic process, granular materials have been effectively used as dampers and protectors [1–10]. For a better understanding of the underlying granular physics, extensive studies have been performed on the wave propagation in granular media. The simplest such systems are one-dimensional (1D) granular chains composed of spheres [2], cylinders [3,4], and more complex particles [5–7]. Solitary waves are usually observed in the chains of monodisperse spherical particles [8]. If the spheres of different diameters or elastic moduli are introduced to the chains, wave reflection and decomposition can occur [9,10]. In the chains of identical cylindrical rods, nonlinear features of contacts and rod vibration lead to more localized solitary waves and stronger energy dissipation compared to the chains of spheres [11,12].

In two-dimensional (2D) and three-dimensional (3D) granular systems, richer phenomena of wave propagation phenomena are observed and show a strong dependence on the spatial arrangements and properties of particles [13–16]. Even a slight variation in packing structure, such as the presence of small gaps due to particle size tolerance in 2D-ordered granular media, can significantly influence wave speeds and peak forces, causing scatter in experimental results [17]. Varying number ratio or stiffness ratio of two granular components can produce diverse wave speeds [18] and wave fronts [19] by redirecting energy transmission within the system, demonstrating a wave-control approach through manipulating composition and topological structure of the granular system.

Compared to systems of rigid spheres and short cylinders, stress wave propagation is much less understood in 3D assemblies of disordered flexible fibers, which have practical applications in lightweight building materials, proppant in oil recovery, and colloidal and granular polymers [20,21]. The fiber systems have complex microstructures with interlocking particle contacts and large particle deformation [20–22], which substantially complicate energy transmission and thus alter the ability of stress attenuation.

In this paper, we find, in experiments and numerical simulations of shock impacts on assemblies of disordered flexible fibers, that the occurrence of solitary or dispersive wave propagation depends on fiber aspect ratio (AR) and flexibility. Stress wave attenuation is remarkably enhanced by dispersive pattern of wave propagation, in which energy trapping due to fiber deformation plays an important role. Thus, the extent of the stress attenuation and wave speed can be modulated by adjusting fiber properties, providing a wave-control and damping technology based on the flexible fibers.

II. METHODOLOGY

A. Experimental setup

In our experiments, as shown in Fig. 1(a), fibers are randomly packed in a cylindrical container and sandwiched between two load cells on which force sensors are installed. A load cell is composed of two acrylic plates, between which a piezoelectric dynamic force sensor is sandwiched. The sensor is secured to the plates using adhesive tape. To prevent the effect of plate deformation on the force measurements, the plates have a large thickness of 10 mm. Four sets of bolts and nuts are used to hold the two plates and the sensor together and apply a precompression force. A steel ball of 4 cm in diameter falls under gravity and impacts the upper load cell at a velocity of 0.4 m/s, generating a shock wave that propagates through the fiber bed from the top to the bottom. The time

*Contact author: yguo@zju.edu.cn

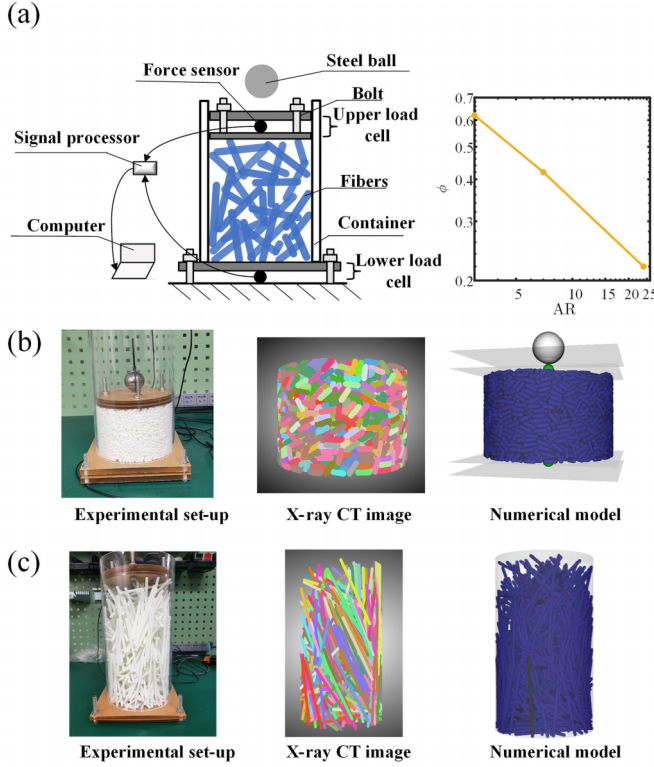


FIG. 1. (a) Schematic plot of experimental setup of a free-falling steel ball impacting a bed of disordered fibers. The inset shows the power law correlation of packing density ϕ and fiber aspect ratio AR for the stiff fibers of $E_b = 7.9 \times 10^9$ Pa in the cylindrical container. Snapshot, x-ray CT image, and numerical model of the packed fibers with fiber aspect ratios of (b) AR = 3 and (c) AR = 24.

evolution of the forces on the upper and lower load cells is automatically recorded by a computer system. To accurately determine time evolution of input and output forces and calculate wave speeds, signals from the upper and lower sensors are synchronized using a signal processor with a sampling frequency of 128 kHz.

The fibers of various ARs are made of photopolymer resin and fabricated using a 3D printing machine. The total solid volume of the fibers packed in the cylindrical container remains the same for various fiber ARs and flexibility. All the fibers have the same diameter, and the number of fibers varies according to the different ARs. In the present experimental impact tests, as shown in the inset of Fig. 1(a), packing density ϕ and fiber aspect ratio AR for the disordered stiff fibers of $E_b = 7.9 \times 10^9$ Pa (made of photopolymer resin) in the cylindrical container follow a power law relationship, which is consistent with the findings of Ref. [20].

The morphology of the fiber beds resolved to single-fiber scale is obtained using a 320 kV x-ray computed tomography (CT) *in situ* testing instrument [see Figs. 1(b) and 1(c)]. To determine the position and orientation of each fiber, as shown in Figs. 1(b) and 1(c), and to analyze the microstructural properties of the fiber packings (e.g., contact force chains), we process the x-ray CT images using the watershed transformation algorithm. This involves filtering, binarizing the images, and applying the watershed transformation to segment

individual fibers [23]. The process is performed using Dragonly software (version 2022.02).

Utilizing the x-ray CT data, high-fidelity numerical models of the fiber beds, which have the same morphology as the experimental setups, can be generated for numerical simulation studies using the discrete element method (DEM).

B. Discrete element method

In the DEM simulations, a semiflexible fiber is represented by a string of bonded spherocylinders, and stretching (compression), bending, and twisting deformations of the fiber are governed by a set of elastic constitutive laws [24,25]. The interactions between fiber-fiber, fiber-plane, and fiber-cylindrical boundaries are modeled as normal and tangential contact forces, described by the modified Hertz-Mindlin models [25]. Viscous dissipation of energies in the contacts and fiber deformations is considered through contact damping and bond-damping forces in the DEM simulations [25]. Additional information about DEM theories is provided in Appendix.

III. RESULTS AND DISCUSSION

A. Speeds and attenuation of stress waves

In the experiments, the forces exerted on the upper load cell, referred to as the source, and the lower load cell, as receiver, are recorded as a function of time [Fig. 2(a)]. The peak force on the receiver F_R^p is remarkably smaller than that on the source F_S^p , indicating significant attenuation in force transmission through the fiber bed. Such force attenuation was also observed in a medium of rigid spheres attributed to Rayleigh scattering and contact damping [26]. As AR increases, the receiver force lasts for a longer time with a decrease in the peak F_R^p . In addition, a smaller force pulse on the source is induced by postshock expansion of the fiber bed at a late time for AR = 24. The similar force attenuation behaviors are obtained for various ARs in the DEM simulations [Fig. 2(b)].

The time instants at which the source and receiver forces reach 20% of the peak receiver force F_R^p (i.e., $0.2F_R^p$) are written as t_S and t_R , respectively, as illustrated in Fig. 2(a). We define the wave speed v_w as

$$v_w = \frac{H}{t_R - t_S}, \quad (1)$$

in which H is the distance between the upper and lower load cells. The time instants t_S^p and t_R^p [Fig. 2(b)] correspond to the peak forces on the source and receiver, respectively. Thus, the speed of peak force v_{pk} is defined as

$$v_{pk} = \frac{H}{t_R^p - t_S^p}. \quad (2)$$

With increasing AR, the wave speed v_w increases [Fig. 2(c)], the speed of peak force v_{pk} decreases [Fig. 2(d)], and the attenuation coefficient, defined as $\alpha = (F_S^p - F_R^p)/F_S^p$, increases [Fig. 2(e)]. These trends are determined by microstructural properties of force transmission paths and mechanism of energy propagation and dissipation, which will be discussed later.

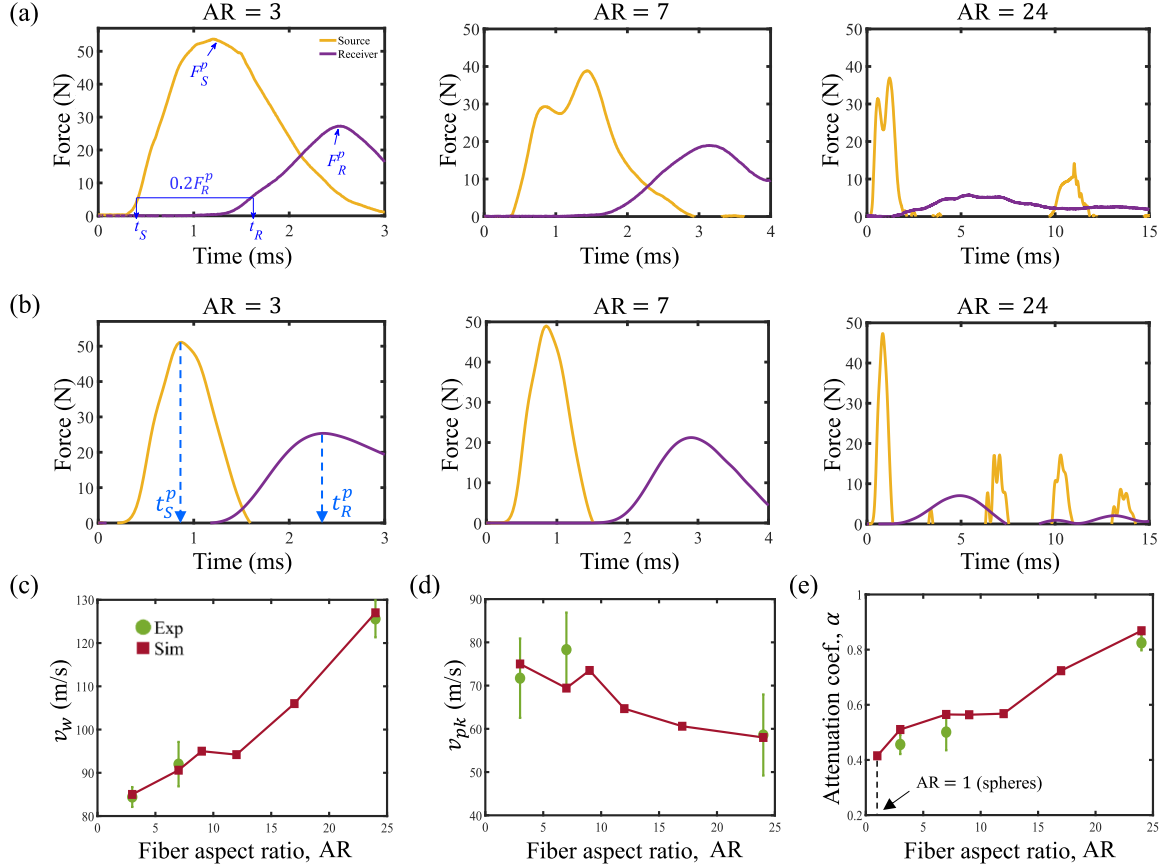


FIG. 2. (a) Experimental and (b) DEM simulation results of forces exerted on the upper load cell (referred to as source) and lower load cell (receiver) as a function of time for the fiber beds with fiber aspect ratios of AR = 3, 7, and 24. Wave speed v_w , speed of peak force v_{pk} , and attenuation coefficient α are plotted as a function of AR in (c)–(e), respectively. Error bars represent SDs across five measurements.

B. Stress wave propagation patterns

To explore the process of stress wave propagation, the fiber bed is equally partitioned into 20 layers in the DEM simulations. Total fiber-fiber contact force F_c , total kinetic energy K , and total potential energy U (due to elastic deformation) of the fibers in each layer can be calculated for a specified time instant. Treating the initial quantities before the impact (F_c^0 , K^0 , and U^0) as the benchmarks, the corresponding incremental contact force $\Delta F_c = F_c - F_c^0$, kinetic energy $\Delta K = K - K^0$, and potential energy $\Delta U = U - U^0$ reflect the changes made by the stress wave.

Spatiotemporal distributions of ΔF_c , ΔK , and ΔU are plotted in Fig. 3, and different patterns of wave propagation are observed for the fiber beds with different fiber aspect ratios. For the short fibers of AR = 3, an inclined, narrow band of ΔF_c is formed at early time [Fig. 3(a)], demonstrating solitary wave propagation. The contact forces drive the movement and deformation of the fibers. Thus, the incremental kinetic energy ΔK and potential energy ΔU transmit in a similar manner as ΔF_c [Figs. 3(d) and 3(g)]. Nevertheless, ΔK lasts longer in the upper region than in the lower region of the bed [Fig. 3(d)]. The wave propagation pattern with AR = 7 [Figs. 3(b), 3(e), and 3(h)] resembles that with AR = 3 [Figs. 3(a), 3(d), and 3(g)], except that stronger attenuation with smaller ΔF_c and ΔK toward the bottom is obtained for AR = 7 compared to AR = 3. It is observed that the potential energy ΔU for

AR = 7 is two orders larger than that for AR = 3, attributed to the larger bending deformation of the larger AR fibers. Thus, as AR increases, more energy is absorbed by the fiber deformation and converted to the potential energy, preventing the propagation of force and energy to the lower region.

Unlike the solitary waves in the short fiber beds with AR = 3 and 7, in the beds of a much larger aspect ratio AR = 24, the stress wave propagates dispersedly with significant contact forces ΔF_c lasting for a much longer duration and remaining primarily in the upper region of the bed [Fig. 3(c)]. Consistently, the energies ΔK and ΔU are trapped in the upper region and hardly propagate to the bottom [Figs. 3(f) and 3(i)]. As a result, lower speeds of the peak force v_{pk} and larger attenuation α are obtained for the larger fiber aspect ratios [Figs. 2(d) and 2(e)] due to the dispersive wave propagation.

C. Shortest percolation force chains

In disordered fiber systems, the microstructures and packing densities of the beds depend on the fiber properties. It can be seen that the packing density decreases with increasing AR in Fig. 1(a). Compared to the one-dimensional ordered fiber chains [11], the disorder leads to diverse packing structures of the elongated fibers with different fiber aspect ratios [Figs. 1(b) and 1(c)] and therefore various microscopic contact structures that determine the transmission of forces

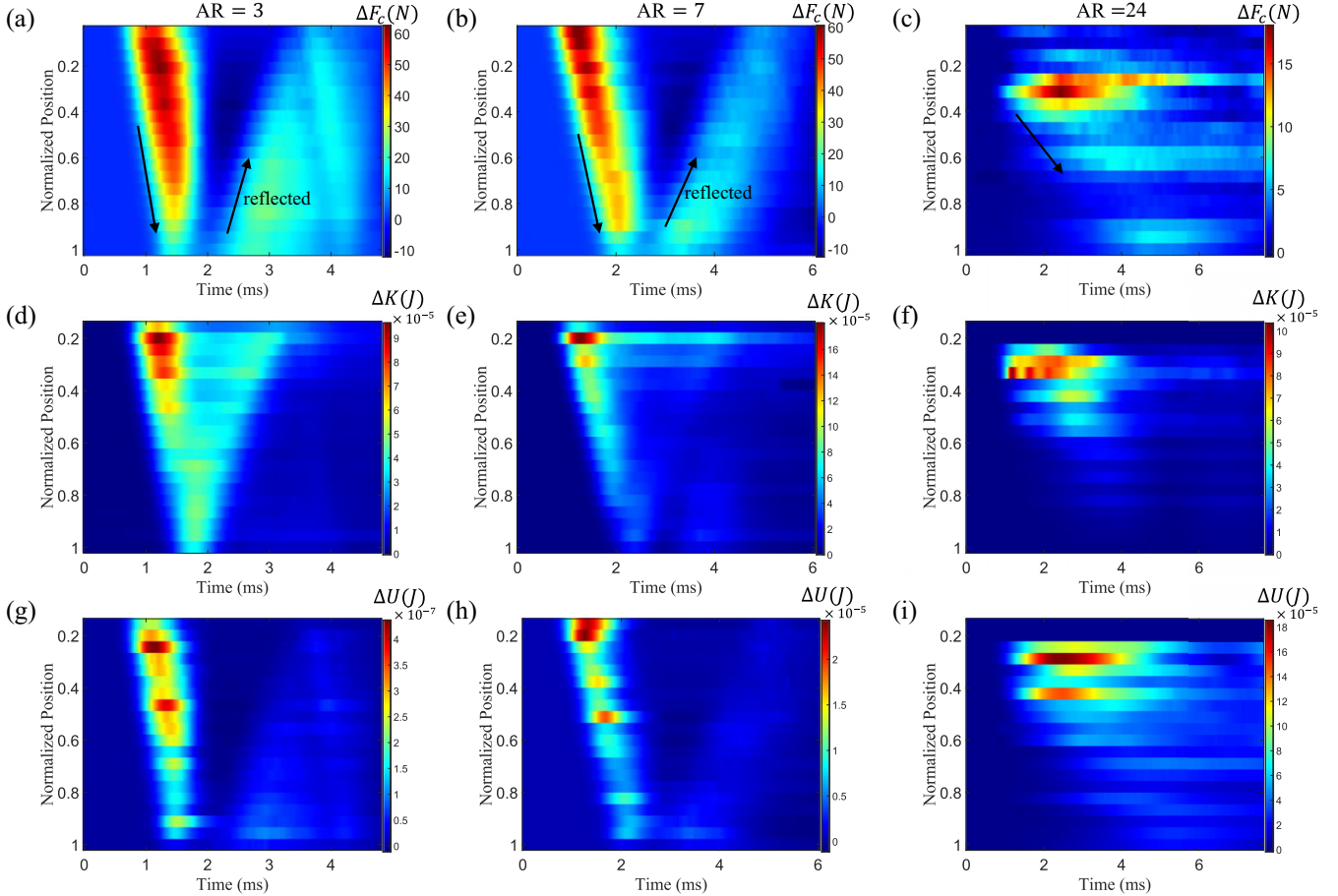


FIG.3. Spatiotemporal distributions of (a)–(c) incremental contact force ΔF_c , (d)–(f) incremental kinetic energy ΔK , and (g)–(i) incremental potential energy ΔU for the fiber beds with fiber aspect ratios of AR = 3, 7, and 24. The present results are obtained from the DEM simulations.

and energies within the fiber bed. Consequently, we trace macroscopic features to microstructural properties of the fiber contact chains. Morphology of the shortest percolation force chain, which is the shortest path between the source and receiver plates in the network of force chains [23,27–29], characterizes the microstructure and connectivity of a granular system [18] and therefore has a crucial impact on the stress wave propagation.

We investigate the effect of force chains on the stress wave propagation by defining a shortest percolation contact force chain, which is the shortest path that allows the force wave to reach the receiver plate in the shortest time duration. The steps to determine the shortest percolation contact force chain in a packed fiber bed are as follows: (1) Identify the first fiber in the chain, which has its center of mass at the highest position in the fiber bed and designate it as the current fiber of interest. (2) Find all the neighboring fibers that are in contact with the current fiber of interest in the chain. (3) From these contacting fibers, select the one with the center of mass at the lowest position and update it as the current fiber of interest. Repeat (2) and (3) until the current fiber of interest touches the bottom receiver plate. The shortest percolation force chain is formed by all these fibers of interest identified in the above procedure. Based on the x-ray CT data of the packed fiber beds in the experiments, the shortest percolation force chains

are determined for the beds with various ARs, as highlighted by the red particles that construct the chains in Fig. 4(a). We also present additional force chains with similar morphology by altering the starting fiber, beginning not from the highest fiber but from the fiber in contact with the source plate, as shown in green and blue in Fig. 4(a).

It is observed that the number of fibers in the shortest force chain N decreases with increasing AR [Fig. 4(b)]. Assuming the average tilting angle of the fibers from the horizontal plane as θ , the projection of a single fiber in the direction of wave propagation (vertical in the present setups) is $AR \cdot d_f \cdot \sin \theta$, in which d_f is fiber diameter. Thus, the smallest number of fibers in the shortest force chain can be written as

$$N = \frac{H_0}{AR \cdot d_f \cdot \sin \theta}, \quad (3)$$

in which H_0 is the fiber bed height between the source and receiver plates and has a correlation with packing density ϕ ,

$$H_0 = \frac{V_f^{\text{total}}}{A_S \cdot \phi}, \quad (4)$$

where V_f^{total} is the total volume of the fibers in the bed and A_S is the cross sectional area of the cylindrical container.

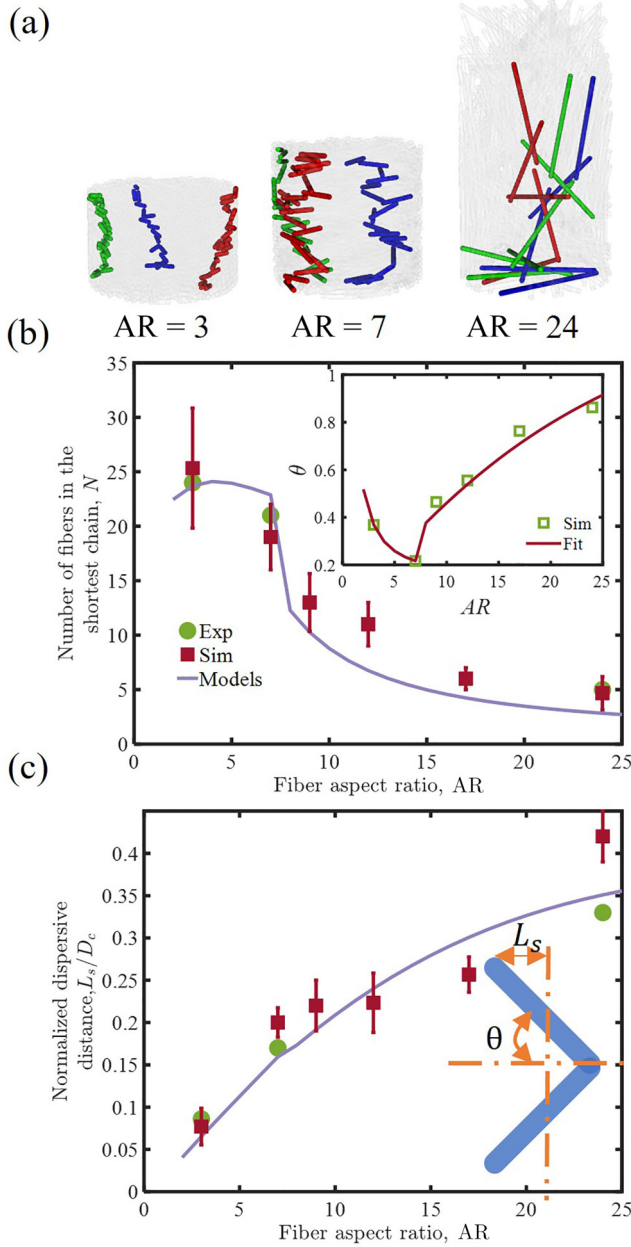


FIG. 4. (a) Shortest percolation force chains (red) obtained from the x-ray CT images in the experiments for $AR = 3, 7$ and 24 . Additional percolation force chains are colored in green and blue for a comparison with the shortest ones. (b) Number of fibers in the shortest force chain N (insert average tilting angle of the fibers θ) and (c) normalized dispersive distance L_s/D_c as a function of fiber aspect ratio AR .

Substituting Eq. (4) to (3) gives

$$N = \frac{V_f^{\text{total}}}{A_s \cdot d_f \cdot AR \cdot \phi \cdot \sin \theta}. \quad (5)$$

For randomly packed, monodisperse rods, the correlation between the packing density ϕ and AR is provided in Ref. [20]. In a bed of disordered short fibers with the fiber aspect ratios (ARs) up to 7, the average tilting angle of the fibers from the horizontal plane θ decreases with increasing AR ,

as described in Ref. [30]. In the present experiments and numerical simulations, an increase in θ with AR is observed for $AR > 7$ as shown in the insert of Fig. 4(b) (open squares), due to the constraints by the boundary of the container on the orientation of the fibers. Thus, a piecewise function is proposed to describe the different behaviors of the AR dependence,

$$\theta = \begin{cases} \tan^{-1}\left(\frac{a}{AR}\right), & AR \leq 7 \\ \tan^{-1}(bAR), & AR > 7, \end{cases} \quad (6)$$

in which a and b are the parameters depending on fiber contact properties (e.g., interfiber friction coefficient and coefficient of restitution) and the size ratio of the container to the fiber length. By fitting to the experimental and numerical data, the model describing the correlation of θ and AR based on Eq. (6) is determined in the inset of Fig. 4(b) (solid line).

Therefore, according to Eq. (5), N can be expressed as a function of AR in Fig. 4(b). In a chain of more fibers, the force pulse needs to transmit through more fiber-fiber contact points, slowing down transmission speed due to small contact areas and dissipative nature of the contacts. Thus, lower wave speeds v_w are obtained for the beds with smaller ARs [Fig. 2(c)], which have a larger numbers of fibers and contacts in their shortest force chains [Fig. 4(b)].

Spatial deviation of a force chain from the propagation direction plays a significant role in dispersing the wave and dissipating the energy. As shown in Fig. 4(c), a dispersive distance L_s is defined as the half length of the projection of a fiber in the transverse (horizontal in the present setups) direction,

$$L_s = \frac{1}{2} AR \cdot d_f \cdot \cos \theta, \quad (7)$$

which is normalized by the diameter of the cylindrical container D_c :

$$\frac{L_s}{D_c} = \frac{AR \cdot d_f \cdot \cos \theta}{2D_c}. \quad (8)$$

As AR increases, the normalized dispersive distance L_s/D_c increases (Fig. 4(c)), enhancing dispersive propagation of forces and energies [Figs. 3(c), 3(f), and 3(i)]. Due to the enhanced dispersive propagation, the forces and energies are trapped in the upper region of the bed, causing a delay in the peak force transmission and a decrease in the peak force speed v_{pk} . The wave speed v_w and peak force speed v_{pk} exhibit opposite trends with respect to AR , as v_w depends on the number of fibers and contacts in the shortest percolation force chain, while v_{pk} is dominated by the dispersive distances of the contact force chains.

D. Effect of fiber flexibility

Flexibility of fibers is characterized by fiber bending modulus E_b , quantifying the capacity to resist fiber bending deformation (see Appendix). The fibers are more flexible with a smaller E_b . In our experiments, stiff fibers with $E_b = 7.9 \times 10^9$ Pa (made of photopolymer resin) and semiflexible fibers with $E_b = 6.6 \times 10^6$ Pa (silicone rubber) are used to investigate the effect of fiber flexibility on the wave propagation [Figs. 5(a) and 5(b)]. More significant attenuation with a much smaller force on the receiver is obtained for the semiflexible fibers [Fig. 5(d)] than the stiff ones [Fig. 5(c)]. It takes a much

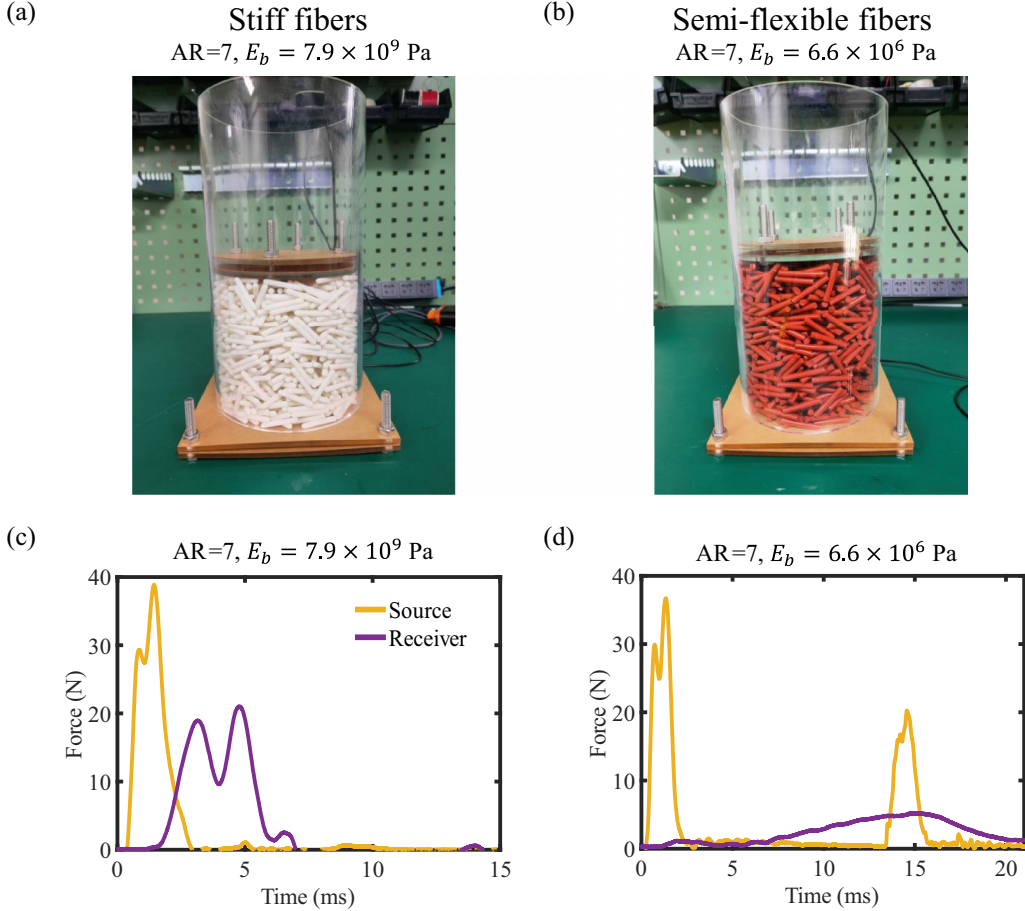


FIG. 5. Experimental setups of impacts on (a) stiff and (b) semiflexible fibers. Experimental results of forces exerted on the source and receiver as a function of time for the beds of (c) stiff and (d) semiflexible fibers.

longer time for the receiver force to reach the peak for the semiflexible fibers, and meanwhile a second force impulse on the source plate occurs due to the postshock expansion of the fiber bed [Fig. 5(d)]. These results demonstrate the excellent ability of energy absorption and shock mitigation for the semiflexible fibers.

The DEM simulations allow us to check the effect of fiber bend moduli E_b spanning a wide range of 10 to 10^{10} Pa. As shown in Fig. 6, the largest attenuation coefficients α and lowest wave speeds v_w are obtained in the beds of semiflexible fibers with 10^2 Pa $< E_b < 10^7$ Pa, through which wave propagates dispersedly as depicted in the spatiotemporal distribution of ΔF_c for $E_b = 6.6 \times 10^6$ Pa. The dispersive wave propagation is attributed to the fact that more energy is trapped in the form of potential energy due to fiber deformation [Figs. 7(d)]. Therefore, most of the kinetic energy ΔK remains in the upper region of the bed and barely transmits downwards [Fig. 7(b)]. As the fibers become stiffer, i.e., $E_b > 10^8$ Pa, the attenuation α decreases and wave speed v_w increases. The small fiber deformation results in a low capacity to store the potential energy [Fig. 3(h)]. In addition, the wave propagates faster within stiff fibers. Thus, a solitary wave is observed in the spatiotemporal distribution of ΔF_c for the stiff fibers.

When the fibers are nearly completely flexible with $E_b < 10^3$ Pa, the bed is consolidated with a large packing density

($\phi = 0.662$ for $E_b = 79$ Pa). Although the packing densities of the quasi-fully-flexible and stiff systems are significantly different, wave propagation patterns are surprisingly similar, as shown in the spatiotemporal distributions in Fig. 6. In the stiff fiber system, the disordered fibers are packed at a lower density of $\phi = 0.437$ with a smaller number of the fiber-fiber contacts. Besides through the contact points, the force transmission through the elongated bodies of the fibers also plays a critical role in the stress wave propagation. Thus, faster force transmission and wave propagation occur with larger stiffness of the fiber material. In contrast to the quasi-fully-flexible system, where packing density is much higher ($\phi = 0.662$) with a much larger contact number, the forces are transmitted primarily through the dense network of the strong contacts. Such strong contacts facilitate the rapid transmission of contact force (Fig. 6) and kinetic energy [Fig. 7(a)] to the bottom receiver plate, leading to higher wave speeds v_w (Fig. 6). In spite of large fiber deformation, the quasi-fully-flexible fibers have a weak capacity to store the potential energy [small magnitudes of ΔU in Fig. 7(c)], due to the very small bending modulus E_b . Thus, solitary wave propagation is obtained in the quasi-fully-flexible fibers, similar to the wave pattern in the stiff fibers, and the force pulse is less reduced with smaller attenuation coefficients α . As a result, it is found that the semiflexible fibers with moderate bending moduli have the best ability to absorb energy and reduce the shock impact.

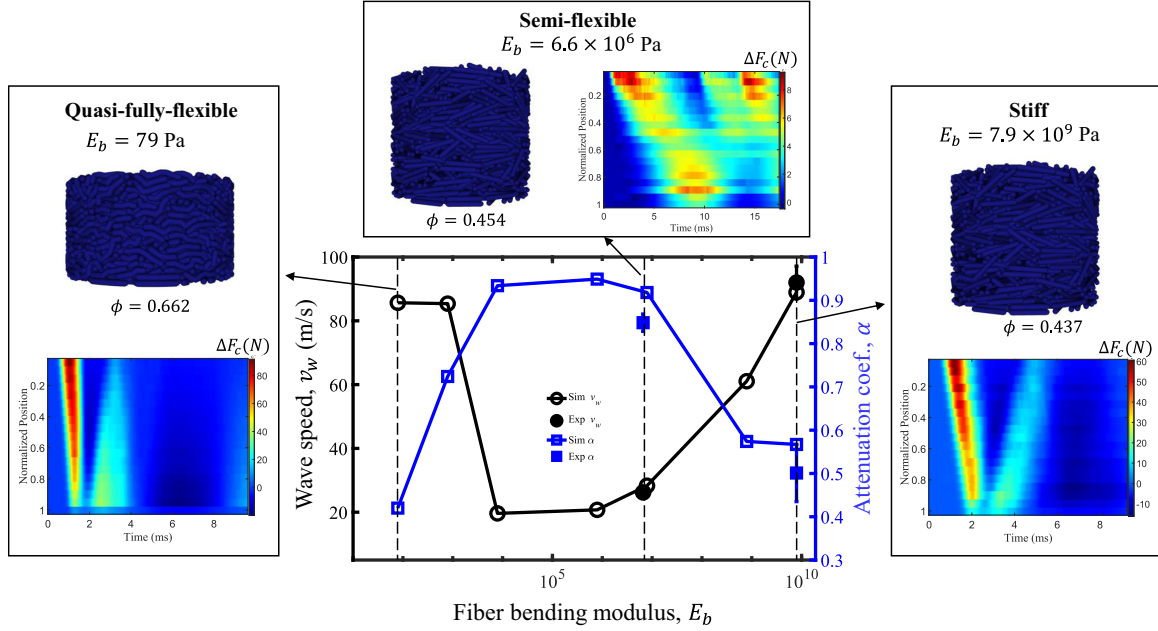


FIG. 6. Wave speed v_w and attenuation coefficient α as a function of fiber bending modulus E_b . The inserts show the snapshots of fiber beds and spatiotemporal distributions of the incremental contact force ΔF_c obtained from the DEM simulations.

In conclusion, we experimentally and computationally elucidate stress wave propagation in packings of disordered flexible fibers. We find that dispersive wave propagation contributes to a large extent of attenuation in forces and energies. A larger fiber aspect ratio leads to fewer fibers in the shortest

percolation force chain, increasing wave speed, and a larger dispersive distance of the force chain, promoting the dispersive wave propagation. Semiflexible fibers with moderate fiber bending moduli E_b have the best capacity to absorb kinetic energy by converting it to potential energy through fiber

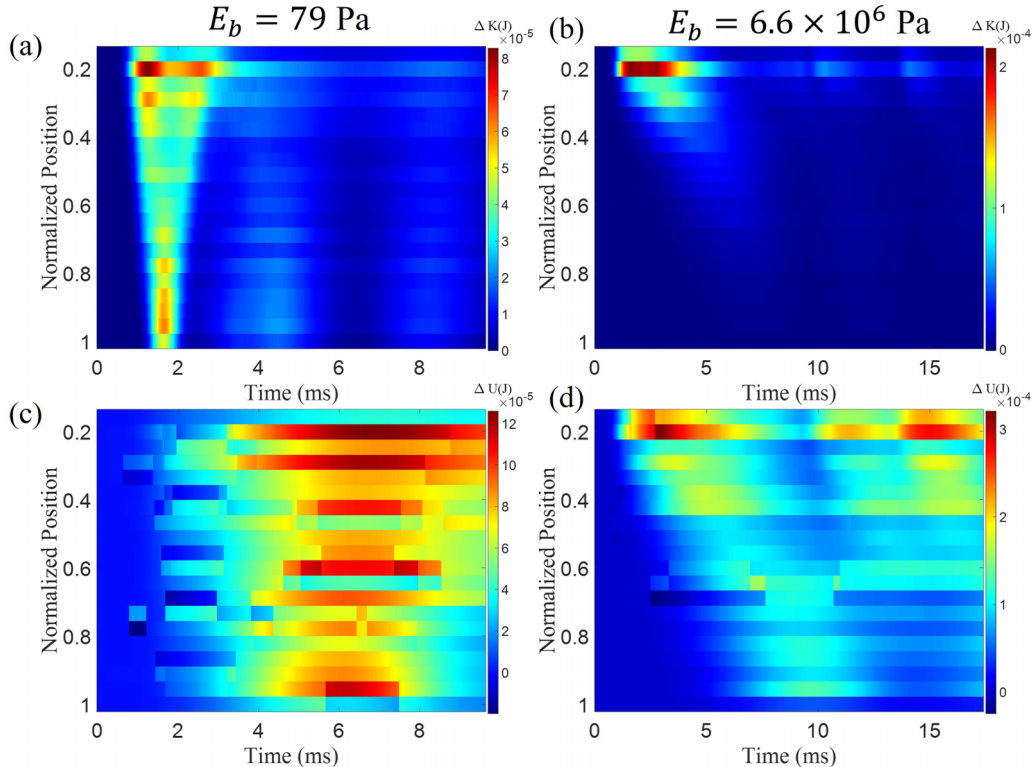


FIG. 7. Spatiotemporal distributions of [(a), (b)] incremental kinetic energy ΔK , and [(c), (d)] incremental potential energy ΔU for the quasi-fully-flexible fibers with a bending modulus of $E_b = 79 \text{ Pa}$ and semiflexible fibers with $E_b = 6.6 \times 10^6 \text{ Pa}$, respectively. All the fibers have the same aspect ratio of $AR = 7$. The present results are obtained from the DEM simulations.

deformation, which is eventually dissipated through interfiber contacts and fiber vibration. Consequently, lower wave speeds and larger attenuation in transmitted forces are obtained for semiflexible fibers compared with stiff fibers and quasi-fully-flexible fibers. The findings in this paper open possibilities for wave-control technology and improved design of energy-absorbing and shockproof materials.

ACKNOWLEDGMENTS

This work was financially supported by the National Natural Science Foundation of China (No. 12372250 and No. 12132015), Zhejiang Provincial Natural Science Foundation of China (No. LZ24A020002), and Specialized Research Projects of Huanjiang Laboratory (No. XYY-128102-E52201).

DATA AVAILABILITY

The data that support the findings of this article are not publicly available upon publication because it is not technically feasible and/or the cost of preparing, depositing, and hosting the data would be prohibitive within the terms of this research project. The data are available from the authors upon reasonable request.

APPENDIX: THEORETICAL ASPECTS OF THE DISCRETE ELEMENT METHOD (DEM) FOR FLEXIBLE FIBERS

In the present DEM simulations, a fiber is represented by a string of bonded spherocylinders and two neighboring spherical nodes are connected by a virtual bond [Fig. 8(a)]. Theoretical details of the numerical method are provided in Refs. [24,25] and summarized here for completeness of the contents. The motion of a fiber is determined by a collective movement of the node spheres, including translational and rotational motion governed by Newton's second law of motion,

$$\begin{aligned} m_i \frac{d\mathbf{v}_i}{dt} = & \mathbf{F}_{ni}^c + \mathbf{F}_{ti}^c + \mathbf{F}_{ni}^b + \mathbf{F}_{ti}^b + \mathbf{F}_{ni}^{cd} \\ & + \mathbf{F}_{ti}^{cd} + \mathbf{F}_{ni}^{bd} + \mathbf{F}_{ti}^{bd} + m_i \mathbf{g} \end{aligned} \quad (\text{A1})$$

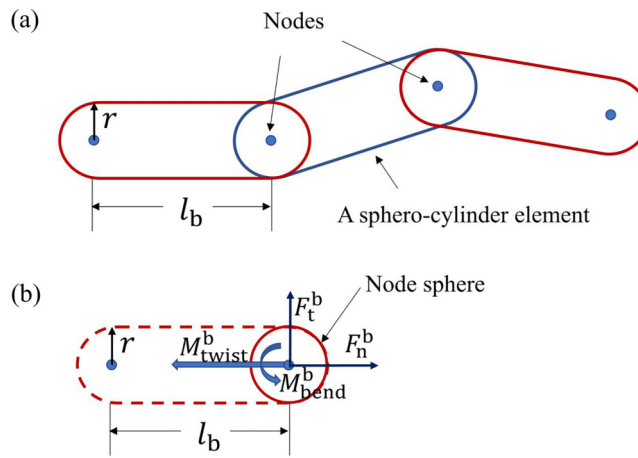


FIG. 8. (a) A sketch of the flexible fiber model and (b) bond forces and moments exerted on a node sphere in the DEM simulations. The images are adopted from Ref. [24].

and

$$J_i \frac{d\omega_i}{dt} = \mathbf{M}_i^c + \mathbf{M}_i^b + \mathbf{M}_i^{cd} + \mathbf{M}_i^{bd}, \quad (\text{A2})$$

in which \mathbf{v}_i and ω_i are the translational and angular velocity vectors, respectively, of node sphere i , with mass m_i and moment of inertia J_i . The translational movement of the node sphere is driven by the normal contact force \mathbf{F}_{ni}^c , tangential contact force \mathbf{F}_{ti}^c , normal bond force \mathbf{F}_{ni}^b , tangential bond force \mathbf{F}_{ti}^b , contact damping forces \mathbf{F}_{ni}^{cd} and \mathbf{F}_{ti}^{cd} , bond-damping forces \mathbf{F}_{ni}^{bd} and \mathbf{F}_{ti}^{bd} , and gravitational force $m_i \mathbf{g}$. Rotational movement is induced by the moments \mathbf{M}_i^c , \mathbf{M}_i^b , \mathbf{M}_i^{cd} , and \mathbf{M}_i^{bd} due to the contact forces, bond forces and moments, contact damping forces, and bond-damping forces and moments, respectively.

The bond forces (F_n^b and F_t^b) and bond moments (M_{twist}^b and M_{bend}^b), as illustrated in Fig. 8(b), are functions of bond deformation, which is described by the relative displacements between two connected node spheres. Hence, the normal and tangential bond forces F_n^b and F_t^b are expressed as linear functions of normal and tangential displacements Δ_n^b and Δ_t^b , respectively,

$$F_n^b = \frac{E_b A}{l_b} \Delta_n^b = K_n^b \Delta_n^b \quad (\text{A3})$$

and

$$F_t^b = \frac{G_b A}{l_b} \Delta_t^b = K_t^b \Delta_t^b. \quad (\text{A4})$$

The bond-twisting moment M_{twist}^b and bond-bending moment M_{bend}^b are computed incrementally based on the relative twisting angular velocity $\dot{\theta}_{twist}$ and relative bending angular velocity $\dot{\theta}_{bend}$ between two connected node spheres,

$$dM_{twist}^b = \frac{G_b I_p}{l_b} \dot{\theta}_{twist} dt = K_{twist}^b \dot{\theta}_{twist} dt \quad (\text{A5})$$

and

$$dM_{bend}^b = \frac{E_b I}{l_b} \dot{\theta}_{bend} dt = K_{bend}^b \dot{\theta}_{bend} dt. \quad (\text{A6})$$

In Eqs. (A3)–(A6), E_b and G_b [$G_b = \frac{E_b}{2(1+v_b)}$, where v_b is the Poisson's ratio of the bond] are the elastic modulus and shear modulus, respectively, of the bond material; A and l_b are the cross-sectional area and length, respectively, of the bond; $I = \pi r^4/4$ is the area moment of inertia; $I_p = \pi r^4/2$ is the polar area moment of inertia; r is the radius of the fiber; and dt is the time step. According to Eq. (A6), the fiber flexibility, indicating the ease for fiber bending deformation, is characterized by the bending modulus E_b : a smaller E_b corresponds to a larger fiber flexibility.

Kinetic energy can be dissipated through deformation and vibration of the flexible fibers. This loss of kinetic energy is considered through bond-damping forces and moments,

$$F_n^{bd} = \beta_b \sqrt{2m_i K_n^b} v_n^r, \quad (\text{A7})$$

$$F_t^{bd} = \beta_b \sqrt{2m_i K_t^b} v_t^r, \quad (\text{A8})$$

$$M_{twist}^{bd} = \beta_b \sqrt{2J_i K_{twist}^b} \dot{\theta}_{twist}, \quad (\text{A9})$$

and

$$M_{\text{bend}}^{\text{bd}} = \beta_b \sqrt{2J_i K_{\text{bend}}^b} \dot{\theta}_{\text{bend}}, \quad (\text{A10})$$

where K_n^b , K_t^b , K_{twist}^b , and K_{bend}^b represent the normal, shear, twisting, and bending stiffnesses, respectively, of the bond as defined in Eqs. (A3)–(A6). The symbols, v_n^r , v_t^r , $\dot{\theta}_{\text{twist}}$, and

$\dot{\theta}_{\text{bend}}$, represent the relative normal velocity, tangential velocity, twisting angular velocity, and bending angular velocity, respectively, between two bonded node spheres of mass m_i and moment of inertia J_i . The kinetic energy dissipation rate due to the deformation and vibration of the flexible fibers is determined by the bond-damping coefficient, β_b : the larger β_b , the faster the energy is dissipated.

-
- [1] R. C. Hidalgo, C. U. Grosse, F. Kun, H. W. Reinhardt, and H. J. Herrmann, *Phys. Rev. Lett.* **89**, 205501 (2002).
 - [2] Z. G. Liu, Y. S. Wang, and G. Huang, *Phys. Rev. E* **99**, 062904 (2019).
 - [3] R. Chaunsali, E. Kim, A. Thakkar, P. G. Kevrekidis, and J. Yang, *Phys. Rev. Lett.* **119**, 024301 (2017).
 - [4] D. Khatri, D. Ngo, and C. Daraio, *Granul. Matter* **14**, 63 (2011).
 - [5] W. Zhang and J. Xu, *Extreme Mech. Lett.* **43**, 101156 (2021).
 - [6] H. Kim, E. Kim, C. Chong, P. G. Kevrekidis, and J. Yang, *Phys. Rev. Lett.* **120**, 194101 (2018).
 - [7] F. Fraternali, M. A. Porter, and C. Daraio, *Mech. Adv. Mater. Struct.* **17**, 1 (2009).
 - [8] S. Sen, J. Hong, J. Bang, E. Avalos, and R. Doney, *Phys. Rep.* **462**, 21 (2008).
 - [9] C. Daraio, V. F. Nesterenko, E. B. Herbold, and S. Jin, *Phys. Rev. Lett.* **96**, 058002 (2006).
 - [10] R. Doney and S. Sen, *Phys. Rev. Lett.* **97**, 155502 (2006).
 - [11] E. Kim, F. Li, C. Chong, G. Theocharis, J. Yang, and P. G. Kevrekidis, *Phys. Rev. Lett.* **114**, 118002 (2015).
 - [12] H. Xu, P. G. Kevrekidis, and A. Stefanov, *J. Phys. A: Math. Theor.* **48**, 195204 (2015).
 - [13] S. van den Wildenberg, R. van Loo, and M. van Hecke, *Phys. Rev. Lett.* **111**, 218003 (2013).
 - [14] E. Kim, Y. H. N. Kim, and J. Yang, *Int. J. Solids Struct.* **58**, 128 (2015).
 - [15] J. Wang, X. Chu, J. Zhang, and H. Liu, *Int. J. Solids Struct.* **159**, 156 (2019).
 - [16] H. Wang, B. Wu, X. Liu, C. He, and L. H. Pueh, *Granul. Matter* **24**, 77 (2022).
 - [17] R. F. Waymel, E. Wang, A. Awasthi, P. H. Geubelle, and J. Lambros, *J. Mech. Phys. Solids* **120**, 117 (2018).
 - [18] K. Taghizadeh, M. Ruf, S. Luding, and H. Steeb, *Proc. Natl. Acad. Sci. USA* **120**, e2219999120 (2023).
 - [19] A. Leonard and C. Daraio, *Phys. Rev. Lett.* **108**, 214301 (2012).
 - [20] K. Desmond and S. V. Franklin, *Phys. Rev. E* **73**, 031306 (2006).
 - [21] R. S. Hoy, *Phys. Rev. Lett.* **118**, 068002 (2017).
 - [22] A. Guerra, A. C. Slim, D. P. Holmes, and O. Kodio, *Phys. Rev. Lett.* **130**, 148201 (2023).
 - [23] Y. Bhosale, N. Weiner, A. Butler, S. H. Kim, M. Gazzola, and H. King, *Phys. Rev. Lett.* **128**, 198003 (2022).
 - [24] Y. Guo, C. Wassgren, J. S. Curtis, and D. Xu, *Chem. Eng. Sci.* **175**, 118 (2018).
 - [25] Y. Guo, Y. Li, Q. Liu, H. Jin, D. Xu, C. Wassgren, and J. S. Curtis, *AIChE J.* **66**, e16946 (2020).
 - [26] C. Zhai, E. B. Herbold, and R. C. Hurley, *Proc. Natl. Acad. Sci. USA* **117**, 16234 (2020).
 - [27] A. Shukla, *Opt. Lasers Eng.* **14**, 165 (1991).
 - [28] D. Howell, R. P. Behringer, and C. Veje, *Phys. Rev. Lett.* **82**, 5241 (1999).
 - [29] E. T. Owens and K. E. Daniels, *EPL* **94**, 54005 (2011).
 - [30] R. C. Hidalgo, I. Zuriguel, D. Maza, and I. Pagonabarraga, *Phys. Rev. Lett.* **103**, 118001 (2009).